Responses to the comments of Reviewer #2:

We would like to thank the anonymous referee for his/her comprehensive review and valuable suggestions. These suggestions help us to present our results more clearly. In response, we have made changes according to the referee's suggestions and replied to all comments point by point. All the page and line number for corrections are referred to the revised manuscript, while the page and line number from original reviews are kept intact.

Comments

This manuscript extends the RegGCAS regional carbon assimilation system to assimilate OCO-2 and OCO-3 XCO_2 retrievals and estimate anthropogenic CO_2 emissions over mainland China during the winter of 2022-2023. The national-scale application, the use of direct satellite XCO_2 constraints, and the combination of an OSSE, ground-based evaluation data, a NOx-proxy comparison, and sensitivity experiments are potentially valuable. The reported regional differences between the Beijing-Tianjin-Hebei region (BTH) and the Yangtze River Delta (YRD), as well as the inferred urban-suburban adjustments and short-term changes around the Spring Festival, are also of broad interest.

However, several methodological and interpretive issues currently prevent a robust assessment of the main conclusions. In particular, the performance of WRF-CMAQ for CO2 transport up to 100 Pa was not well evaluated; the state-vector design and its temporal evolution are insufficiently described; correlated and systematic errors in the OCO retrievals are not adequately addressed; the OSSE is close to a perfect-model twin experiment; atmospheric transport errors are not evaluated; and the reported uncertainty of 5.6% is not statistically well justified. In addition, some of the fine-scale spatial and causal interpretations appear stronger than the evidence presented. I therefore recommend major revision. Addressing the points below would substantially improve the study's reliability, reproducibility, and interpretation.

Response: We thank the reviewer for these constructive comments. Regarding the evaluation of full-column CO_2 transport in WRF–CMAQ, we have supplemented the model configuration details, conducted a sensitivity experiment with enhanced vertical resolution, and evaluated simulated vertical CO_2 profiles against CONTRAIL observations. Details are provided in our response to Major Comment 1.

The state vector comprises anthropogenic and biogenic CO_2 flux subvectors, whose prior errors are assumed to be uncorrelated. This treatment follows previous studies that jointly optimized anthropogenic and biogenic fluxes without prescribing prior error correlations between them (Boschetti et al., 2018; Ponomarev et al., 2026). In each subsequent assimilation window, anthropogenic prior emissions inherit the preceding posterior estimates, while biogenic prior fluxes are rebuilt from the corresponding flux product (Jiang et al., 2021). Each ensemble member's final CO_2 concentration field initializes the next window. We have clarified this treatment in the revised manuscript.

See Lines 205–210, Page 7.

"In this study, the ensemble square root filter (EnSRF) was used to jointly optimize anthropogenic and biogenic CO_2 fluxes (Whitaker and Hamill, 2002). The state vector comprises anthropogenic and biogenic flux subvectors, whose prior errors are assumed to be uncorrelated. This treatment follows previous studies that jointly optimized these fluxes without prescribing prior error correlations between them (Boschetti et al., 2018; Ponomarev et al., 2026)."

See Lines 280–284, Pages 9-10.

"Prior biogenic carbon fluxes were derived from the net ecosystem production (NEP) simulated by the Boreal Ecosystem Productivity Simulator (BEPS) model (Wang et al., 2021) at $0.073^{\circ} \times 0.073^{\circ}$ resolution. In each subsequent assimilation window, prior biogenic fluxes were rebuilt from the corresponding flux product (Jiang et al., 2021)."

When assimilating OCO observations, we used the official bias-corrected XCO_2 products and retained only Land Nadir and Land Glint retrievals with valid XCO_2 values that passed the quality-flag screening. To mitigate the effects of correlated retrieval errors, we averaged soundings within each model grid cell over the corresponding time interval into a single super-observation, following similar approaches in previous studies (Jiang et al., 2022; Byrne et al., 2024). The assigned uncertainty was the arithmetic mean of the reported sounding uncertainties, helping limit the risk of over-weighting densely sampled observations. We have clarified these procedures in the revised manuscript.

See Lines 310–318, Page 10.

"Nearby OCO-2/3 soundings can have correlated retrieval errors, with OCO-2 along-track error correlation scales of approximately 10 and 20 km reported by Baker et al. (2022). We therefore aggregated these soundings before assimilation. After screening them according to the assimilation time window, we averaged the XCO_2 values within each 27 km model grid cell to form a single super-observation (Jiang et al., 2022; He et al., 2023; Byrne et al., 2024). For the EnSRF assimilation, the observation error standard deviation for each super-observation was estimated based on the reported retrieval uncertainties of the contributing soundings (Jiang et al., 2022). The spatial distribution and counts of the super-observations are shown in Fig. 3."

Regarding the OSSE, we acknowledge that the original design is idealized, particularly in its assumption of a spatially uniform 30% underestimate in prior emissions. We therefore conducted an additional OSSE with spatially heterogeneous prior errors, retaining MEIC emissions as the truth. The prior was constructed by adding spatially varying Gaussian noise to 70% of MEIC emissions, with a standard deviation equal to 25% of MEIC emissions at each grid cell. All other settings remained unchanged. As shown in Fig. S7, the inversion generally reduced the widespread underestimation over eastern China, although substantial biases remained in some grid

cells. Absolute errors in regional emission totals decreased by 66.6%, 95.6%, and 59.1% over mainland China, BTH, and the YRD, respectively. These reductions were comparable to those in the original OSSE (67.8%, 98.7%, and 57.9% for mainland China, BTH, and the YRD, respectively). Posterior totals differed from the original results by less than 1% in all three regions. These results indicate that the inversion remained effective in improving regional emission totals after spatially heterogeneous prior errors were introduced. The results of this experiment have been added to the Supplement (Text S4 and Fig. S7).

"**Supplement**

Text S4 OSSE with spatially heterogeneous prior emission errors

To assess the sensitivity of emission recovery to spatially heterogeneous prior errors, we conducted an additional OSSE by adding grid-cell Gaussian noise to the prior emissions used in the original experiment. The perturbed prior emissions were constructed as:

$$E_{prior,i} = 0.70E_{MEIC,i} + 0.25E_{MEIC,i}\xi_i, \qquad \xi_i \sim N(0,1).$$

Where $E_{prior,i}$ denotes the perturbed prior emissions in grid cell i, $E_{MEIC,i}$ denotes the corresponding MEIC emissions, and ξ_i is a standard normally distributed random variable. The coefficient 0.25 sets the standard deviation of the perturbation to 25% of the MEIC emissions in each grid cell.

The inversion generally reduced the widespread negative emission biases over eastern China, although substantial residual biases remained in some grid cells (Fig. S7). Absolute errors in regional emission totals decreased by 66.6%, 95.6%, and 59.1% over mainland China, BTH, and the YRD, respectively. These reductions were comparable to those in the original OSSE (68.0%, 98.7%, and 58.0%, respectively). Posterior emission totals differed by less than 1% between the two experiments in all three regions, indicating that regional estimates were relatively insensitive to the tested grid-cell perturbations."

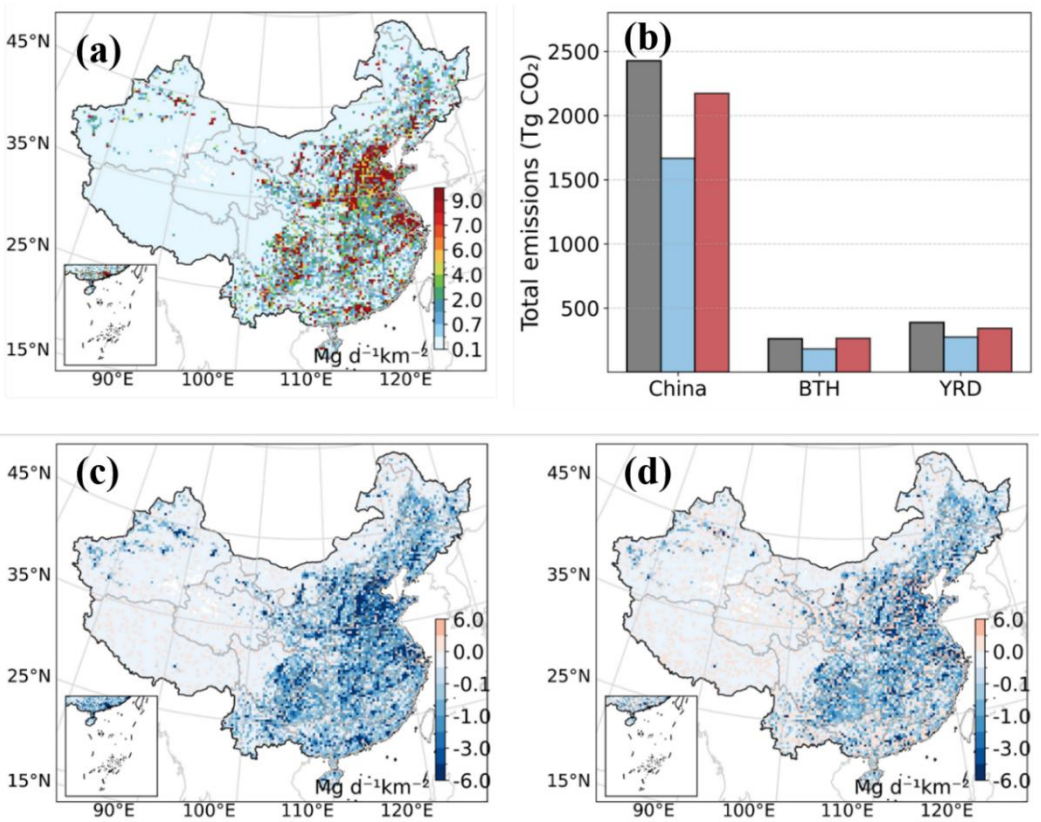


Figure S7 Results of the OSSE with spatially heterogeneous prior errors: (a) posterior CO_2 emissions, (b) regional emission totals for the truth, prior, and posterior, (c) prior minus true emissions, and (d) posterior minus true emissions.

Moreover, we evaluated the meteorological fields driving CO_2 transport against observations of wind speed, temperature, and relative humidity. The simulations generally captured the observed temporal variations but overestimated wind speed (Fig. S1). This overestimation can enhance CO_2 ventilation and weaken simulated concentration enhancements, potentially leading the inversion to overestimate emissions to compensate (Ye et al., 2020). We also assessed the sensitivity of posterior emissions to atmospheric transport errors by replacing FNL with ERA5 (Fig. S8). This replacement changed the national posterior emission total by 4.9%, indicating relatively low sensitivity of national posterior emissions to the change in meteorological fields. We also revised the calculation of the overall uncertainty in posterior emissions to combine the posterior ensemble spread with uncertainty contributions estimated from the sensitivity experiments. The experimental setup, results, and revised uncertainty

calculation are detailed in our response to Major Comment 3.

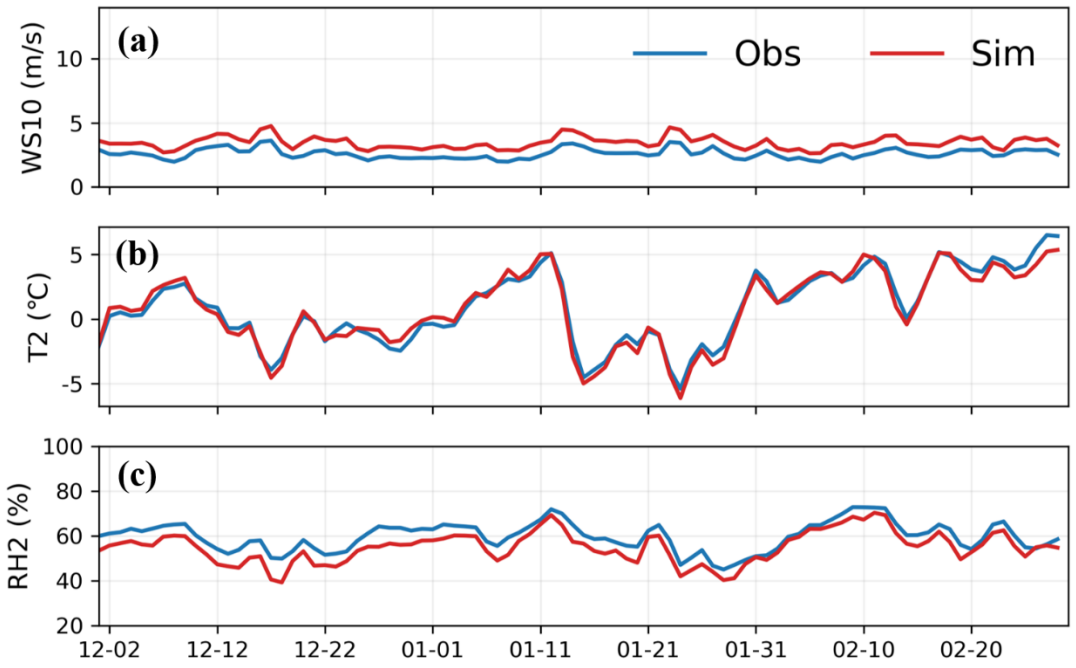


Figure S1 Time series of the observed and simulated wind speeds at 10 m (WS10, m/s), temperature at 2 m (T2, ℃) and relative humidity at 2 m (RH2, %) over mainland China.

See Lines 173–178, Page 6.

"The simulated meteorological fields were evaluated against observations of wind speed, temperature, and relative humidity. The simulations generally reproduced the observed temporal variations, although wind speeds were overestimated (Fig. S1). Overestimated wind speeds can enhance CO_2 ventilation and reduce simulated concentration enhancements. This may lead the inversion to overestimate emissions to compensate (Ye et al., 2020)."

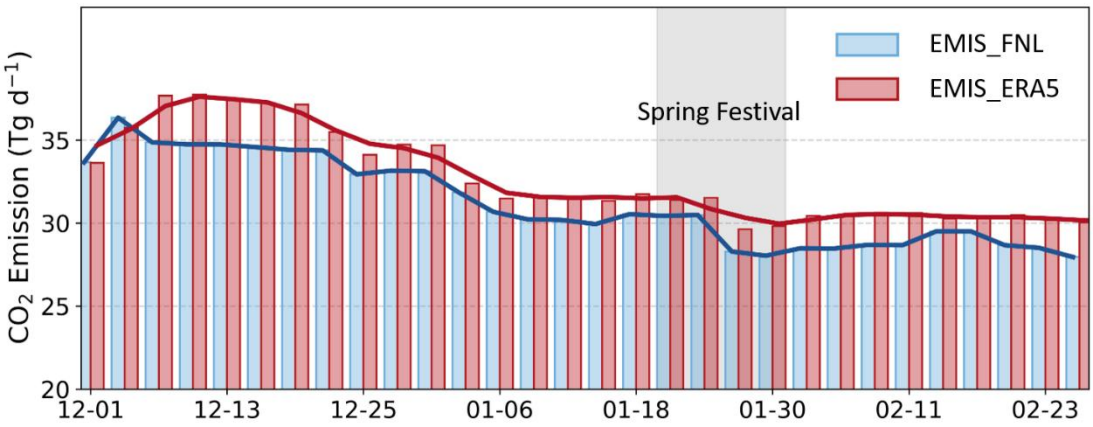


Figure S8 Time series of posterior anthropogenic CO_2 emissions over mainland China using FNL and ERA5 meteorological forcing during winter 2022–2023. The shaded area indicates the Spring Festival holiday.

Regarding the available evidence supporting certain fine-scale spatial patterns, we updated the NO_2-proxy estimates using recent MEICv2 CO_2-to-NO_X emission ratios for the corresponding months of 2022–2023. The updated estimates and direct XCO_2 assimilation show broadly similar spatial features, including downward adjustments in many urban centers and upward adjustments in surrounding areas, although their magnitudes and spatial extents differ. These shared patterns provide indirect qualitative support for the inferred urban–suburban differences. The updated comparison and revised discussion are presented in the manuscript.

See Lines 472–492, Page 16.

"This study also estimates anthropogenic CO_2 emissions using a NO_2-proxy method, with monthly CO_2-to-NO_X emission ratios from MEICv2 for December 2022–February 2023 (Fig. 2). In BTH, both methods yield relatively high emissions in southern Hebei and the Beijing–Tianjin–Tangshan area and lower emissions in northern Hebei. The main emission adjustments occur near major cities and their surrounding areas, with decreases near many urban centers and increases in parts of the surrounding areas. Compared with direct XCO_2 assimilation, the NO_2-proxy method produces more

extensive decreases around Beijing and Tianjin and stronger increases in parts of central and southern Hebei. These differences may partly reflect uncertainties in the CO_2-to-NO_X emission ratios, which depend on sectoral composition and pollution control technologies (Miyazaki and Bowman, 2023; Li et al., 2023). In the YRD, both methods showed emission decreases around southern Jiangsu and Shanghai, with localized reductions also occurring in parts of Zhejiang. Similar urban–suburban adjustment patterns were observed, as in the BTH region. However, the NO_2-proxy method produced more pronounced spatial adjustments and yielded a higher regional emission total than direct XCO_2 assimilation. Satellite XCO_2 observations were available in only 14 assimilation windows over the YRD, fewer than half of the total, providing limited temporal coverage for constraining regional emissions. By comparison, observations covered 70% of the assimilation windows in BTH, where the two methods yielded closer regional emission totals. Overall, the comparison provides additional qualitative support for the emission adjustment patterns in key regions and highlights the need for more observational constraints in the YRD."

Major Comments

1. Validation of CO_2 transport and stratosphere-troposphere exchange in WRF-CMAQ: The manuscript assumes that WRF-CMAQ can accurately transport CO_2 throughout the atmospheric column using only 25 layers between the surface and 100 Pa. However, CMAQ has been developed and evaluated primarily for tropospheric air pollutants, and the applicability of this particular CMAQ v5.0.2 configuration to full-column CO_2 transport is not established in the manuscript. Previous CMAQ studies of stratosphere-troposphere exchange have generally focused on ozone and have used dedicated treatments and extensive evaluation against ozonesonde, aircraft, and satellite observations. Such studies do not by themselves validate passive CO_2 transport in the present configuration.

This issue is important because errors in upper-tropospheric and stratospheric transport,

vertical mixing, or the model-top boundary condition may produce XCO_2 biases that the assimilation subsequently compensates for by adjusting surface anthropogenic emissions. The relatively large sensitivity of the posterior emissions to the prescribed background field further demonstrates this potential ambiguity.

Please provide appropriate references demonstrating that the selected WRF-CMAQ configuration has previously been validated for full-column CO_2 transport, including stratosphere-troposphere exchange. If no such validation exists, the manuscript should provide a dedicated evaluation. At a minimum, the authors should report the complete vertical-layer structure, the number of layers around and above the tropopause, any layer collapsing performed by MCIP, the upper-boundary treatment for CO_2, and the conservation properties of the vertical remapping. A sensitivity experiment with enhanced vertical resolution, particularly in the upper troposphere and lower stratosphere, should quantify the resulting changes in modeled XCO_2 and posterior emissions. Comparison of simulated vertical CO_2 profiles with aircraft, AirCore, or other available profile observations, or with an independently validated high-vertical-resolution transport model, would substantially strengthen the study.

Response: We thank the reviewer for these constructive comments. We clarify that our configuration does not explicitly simulate full-column CO_2 transport. CMAQ simulates CO_2 transport below the model top, and the OCO a priori CO_2 profile is used above it. Simulated XCO_2 is constructed from these combined profiles using the original full-column pressure weights without renormalization.

Previous studies have used CMAQ to simulate atmospheric CO_2 transport and evaluated the resulting column-averaged and surface concentrations against observations. Villalobos et al. (2021) used WRF–CMAQ v5.3 with a model top of 50 hPa. They treated CO_2 as an inert species and assimilated OCO-2 XCO_2 to estimate Australian carbon fluxes. They evaluated the simulations against independent TCCON and surface observations. Kou et al. (2023) used RAMS-driven CMAQ with 15 layers extending to approximately 23 km, well above the tropopause and into the lower stratosphere. They assimilated GOSAT XCO_2 over China and evaluated the results against withheld GOSAT data and observations from 14 surface sites. These studies

provide observational evaluations of CMAQ-based regional CO_2 modelling and inversion, but do not specifically establish the accuracy of CO_2 transport across the tropopause. Column and surface comparisons alone cannot isolate errors in upper-tropospheric and stratospheric transport.

In our system, CMAQ uses 25 nonuniform vertical layers extending from the surface to a model-top pressure of 100 Pa. To document the vertical resolution throughout the model column, we have added Table S2. It lists the lower and upper vertical-coordinate interfaces, layer-center pressure, lower- and upper-interface heights above ground level, and thickness of each layer.

To quantify the number of layers above the tropopause, we identified the first lapse-rate tropopause from WRF temperature profiles at each grid cell and output time. We applied the WMO criterion, which requires a local lapse rate of $\leq$2 K km^{-1}. The mean lapse rate between that level and every evaluated level within 2 km above must also satisfy this threshold (Reichler et al., 2003; Xian and Homeyer, 2019). We then compared the diagnosed tropopause heights with the CMAQ layer interfaces. Using the assimilation window dated 1 December 2022 as an example, we compiled statistics from all valid grid samples over the Chinese land region. The median number of CMAQ layers lying entirely above the tropopause was 3, with a 5th–95th percentile range of 1–6. This count excludes the layer crossing the tropopause.

Regarding the vertical processing by MCIP, the 50 WRF mass layers were mapped onto 25 prescribed CMAQ layers. MCIP performs layer collapsing through vertical interpolation of meteorological fields (Otte and Pleim, 2010). In our configuration, the lower and upper η values in Table S2 define the target layer boundaries. These boundaries do not all coincide with the original WRF interfaces. Linear interpolation in the model vertical coordinate was used to obtain values at the target positions. Layer-centered variables were interpolated from the surrounding WRF layer centers, while interface-defined variables were interpolated from the surrounding WRF interfaces.

At the model top, the vertical advection scheme applies a column mass-continuity correction that yields zero upper-boundary mass flux in exact arithmetic. This is

consistent with the no-exchange treatment described for CMAQ by Lee et al. (2017). Any nonzero residual advective flux is handled using values from the uppermost layer, without prescribing an external CO_2 concentration. Vertical diffusion uses the ACM2 scheme (Pleim, 2007), with a zero-flux boundary condition at the model top. The uppermost-layer CO_2 concentration evolves through transport within the model domain rather than being fixed to a prescribed value.

Regarding conservation, MCIP maps meteorological fields from the WRF levels to the prescribed CMAQ levels through vertical interpolation (Otte and Pleim, 2010). In our implementation, this uses linear interpolation in the model vertical coordinate rather than conservative redistribution of layer-integrated quantities. The procedure therefore does not explicitly enforce column-integral conservation.

To evaluate CMAQ's ability to simulate vertical CO_2 profiles, we compared concentrations simulated using prior emissions with independent CONTRAIL aircraft observations (Machida et al., 2008). The evaluation included 146 ascent/descent profiles collected within the model domain during the study period, primarily around Japan. Model output was collocated with the observations in space and time and vertically interpolated to the measured pressures. The simulated CO_2 profiles showed an overall mean bias of 0.4 ppm relative to CONTRAIL observations (Fig. S2). Agreement was closer in the middle and upper troposphere, where RMSEs were 2.0 ppm at 300–600 hPa and 1.5 ppm at 150–300 hPa.

To assess the effects of vertical resolution on modeled XCO_2 and posterior emissions, we conducted a sensitivity experiment that increased the number of CMAQ layers from 25 to 40. The lowest 15 layers, from the surface to $\eta = 0.550$, were retained. Above this interface, additional interfaces subdivided the original 10 layers into 25 layers, refining the upper troposphere and lower stratosphere. The model-top pressure remained at 100 Pa. The vertical configurations are compared in Table S3. Compared with the original 25-layer experiment, the 40-layer experiment produced small changes in simulated XCO_2. The mean difference was 0.03 ppm, with an RMSE difference of 0.2 ppm. The broad spatial distribution of XCO_2 remained similar, and the fit to

observations was nearly unchanged (Fig. S3). National posterior anthropogenic CO_2 emissions decreased by 0.6%, with regional changes of −3.1% over BTH and +1.0% over the YRD. Spatial differences included both increases and decreases over eastern China, while the main emission patterns were retained. The national emission time series also remained similar, including the decline during the Spring Festival. These results indicate that the regional emission totals and their temporal variations were relatively insensitive to the vertical refinement. Comparison with independent CONTRAIL aircraft observations showed that both configurations captured the observed decrease in CO_2 with altitude (Fig. S4). The overall RMSE and mean bias were 3.29 and 0.6 ppm for the 25-layer configuration, and 3.33 and 0.7 ppm for the 40-layer configuration. At 150–300 hPa, the 25-layer configuration had a mean bias of 0.9 ppm and an RMSE of 1.6 ppm. The corresponding values for the 40-layer configuration were 1.1 and 1.7 ppm. The largest discrepancy occurred in the 950–1000 hPa bin, where both configurations underestimated CO_2 by approximately 10.7 ppm. This near-surface discrepancy may be related to local anthropogenic emissions and uncertainties in boundary-layer mixing (Niwa et al., 2012; Verma et al., 2017). However, only six profiles contributed to this bin, limiting its representativeness. These results indicate limited sensitivity of the simulated CO_2 profiles to the tested vertical refinement. The original 25-layer configuration performed slightly better overall in this comparison.

To assess the sensitivity of posterior emissions to model-top height, we performed an additional inversion with the CMAQ model top lowered from 1 to 50 hPa. National posterior anthropogenic CO_2 emissions decreased by 4.6% relative to BASE, indicating limited sensitivity to model-top height.

We have expanded the model description and summarized the sensitivity experiments and evaluation in the revised manuscript. Detailed configurations, methods, and results are provided in the Supplement.

See Lines 165–172, Page 6.

"Vertically, 25 sigma-pressure layers were set from the surface up to 100 Pa. The complete vertical-layer structure is provided in Table S2. The median number of

CMAQ layers lying entirely above the tropopause was 3 over the Chinese land region, with a 5th–95th percentile range of 1–6. Meteorological fields from 50 WRF layers were mapped to 25 CMAQ layers using linear vertical interpolation, without explicitly enforcing column-integral conservation. At the model top, vertical advection uses a column mass-continuity correction to impose a zero-flux upper boundary, while vertical diffusion also applies a zero-flux boundary condition."

See Lines 191–200, Page 7.

"Additionally, we evaluated CMAQ-simulated CO_2 profiles driven by prior emissions against independent CONTRAIL aircraft observations (Machida et al., 2008; Fig. S2). The evaluation showed an overall mean bias of 0.4 ppm and an RMSE of 3.2 ppm. Agreement was closer in the middle and upper troposphere, with RMSEs of 2.0 ppm at 300–600 hPa and 1.5 ppm at 150–300 hPa. We also conducted a sensitivity experiment with enhanced vertical resolution, particularly in the upper troposphere and lower stratosphere. The evaluation results are presented in the Supplement (Text S1; Fig. S3). Increasing the number of layers from 25 to 40 decreased national posterior emissions by only 0.6%, while the main spatial patterns and temporal variations remained similar, indicating limited sensitivity to vertical resolution."

"**Supplement**

Text S1 Evaluation against CONTRAIL aircraft CO_2 profiles

We conducted a sensitivity experiment that increased the number of CMAQ layers from 25 to 40, with enhanced resolution particularly in the upper troposphere and lower stratosphere. The lowest 15 layers and the model-top pressure of 100 Pa were retained. Above these layers, the number of layers increased from 10 to 25. The corresponding vertical configurations are compared in Table S2.

To evaluate the simulated vertical CO_2 distribution, we used independent

CONTRAIL aircraft observations collected during the study period (Machida et al., 2008). The evaluation included 146 ascent/descent profiles within the model domain, primarily around Japan. Each observation was matched to the corresponding model grid cell and hourly output. Simulated CO_2 was linearly interpolated in log pressure to the observed pressure. Composite profiles were constructed in 50 hPa bins by first averaging each ascent/descent segment within each bin and then assigning equal weight to the segment means. Bias and RMSE were calculated from the matched segment means within the pressure bins.

The simulations captured the observed decrease in CO_2 with altitude. The overall RMSE and mean bias were 3.29 and 0.6 ppm for the original configuration, and 3.33 and 0.7 ppm after refinement. At 150–300 hPa, the original configuration had a mean bias of 0.9 ppm and an RMSE of 1.6 ppm, compared with 1.1 and 1.7 ppm after refinement. The largest discrepancy occurred in the 950–1000 hPa bin, where both configurations underestimated CO_2 by approximately 10.7 ppm. This discrepancy may be related to local anthropogenic emissions and uncertainties in boundary-layer mixing (Niwa et al., 2012; Verma et al., 2017). Only six profiles contributed to this bin (Fig. S3). Overall, simulated CO_2 profiles showed limited sensitivity to the tested vertical refinement, and the original configuration performed slightly better in this comparison.

Text S2 Sensitivity to enhanced vertical resolution

Using the refined configuration described in Text S1, we further assessed the sensitivity of posterior anthropogenic CO_2 emissions to enhanced vertical resolution. Relative to the original experiment, simulated XCO_2 increased by 0.03 ppm on average, with an RMSE difference of 0.2 ppm. The broad spatial distribution and agreement with satellite observations remained similar (Fig. S4 a–b). National posterior anthropogenic CO_2 emissions decreased by 0.6%, with changes of −3.1% over BTH and 1.0% over the YRD. Local increases and decreases occurred over eastern China, while the main

spatial patterns and national temporal variations were retained, including the decline during the Spring Festival (Fig. S4 c–e). These results indicate limited sensitivity of the national winter emission estimate to the tested vertical refinement."

Table S2 Complete vertical-layer structure of the CMAQ transport model.

Layer	Lower-interface η	Upper-interface η	Pressure (hPa)	Lower-interface height (km)	Upper-interface height (km)	Thickness (km)
1	1.00000	0.99381	890.76	0	0.05	0.05
2	0.99381	0.98800	885.42	0.05	0.09	0.04
3	0.98800	0.98100	879.74	0.09	0.15	0.06
4	0.98100	0.97200	872.67	0.15	0.22	0.07
5	0.97200	0.96000	863.44	0.22	0.32	0.1
6	0.96000	0.94400	851.19	0.32	0.44	0.12
7	0.94400	0.92200	834.7	0.44	0.63	0.19
8	0.92200	0.89400	813.17	0.63	0.86	0.23
9	0.89400	0.86000	786.8	0.86	1.16	0.3
10	0.86000	0.82000	755.64	1.16	1.51	0.35
11	0.82000	0.77200	719.01	1.51	1.96	0.45
12	0.77200	0.71800	676.91	1.96	2.5	0.54
13	0.71800	0.66200	631.74	2.5	3.08	0.58
14	0.66200	0.60600	585.74	3.08	3.7	0.62
15	0.60600	0.55000	539.5	3.7	4.36	0.66
16	0.55000	0.49400	492.74	4.36	5.08	0.72
17	0.49400	0.43800	445.22	5.08	5.85	0.77
18	0.43800	0.38200	396.64	5.85	6.71	0.86
19	0.38200	0.32600	346.76	6.71	7.69	0.98
20	0.32600	0.27000	295.33	7.69	8.81	1.12
21	0.27000	0.21400	242.07	8.81	10.15	1.34
22	0.21400	0.15800	186.81	10.15	11.87	1.72
23	0.15800	0.10200	130.87	11.87	14.3	2.43
24	0.10200	0.04800	75.93	14.3	18.43	4.13
25	0.04800	0.00000	24.98	18.43	39.41	20.98

Notes: Layers are numbered upward from the surface. Pressures refer to layer centers, and heights are above ground level. The model-top pressure is 100 Pa (1 hPa). Values are calculated from data over the Chinese land region for the assimilation window dated 1 December 2022. Layer thickness is the difference between the reported upper- and lower-interface heights.

Table S3 Comparison of vertical discretization between the baseline and enhanced-resolution CMAQ configurations.

η interval	Baseline layers	Refined layers
1.000 – 0.550	15	15
0.550 – 0.326	4	8
0.326 – 0.270	1	2
0.270 – 0.214	1	2
0.214 – 0.158	1	2
0.158 – 0.102	1	3
0.102 – 0.048	1	4
0.048 – 0.000	1	4
Total layers	25	40

Notes: Both configurations extend from the surface to 100 Pa. The lowest 15 layers are unchanged. Additional interfaces subdivide the original layers above η=0.550. Additional η interfaces: 0.522, 0.466, 0.410, 0.354, 0.298, 0.242, 0.186, 0.130, 0.116, 0.088, 0.075, 0.061, 0.030, 0.018, and 0.010.

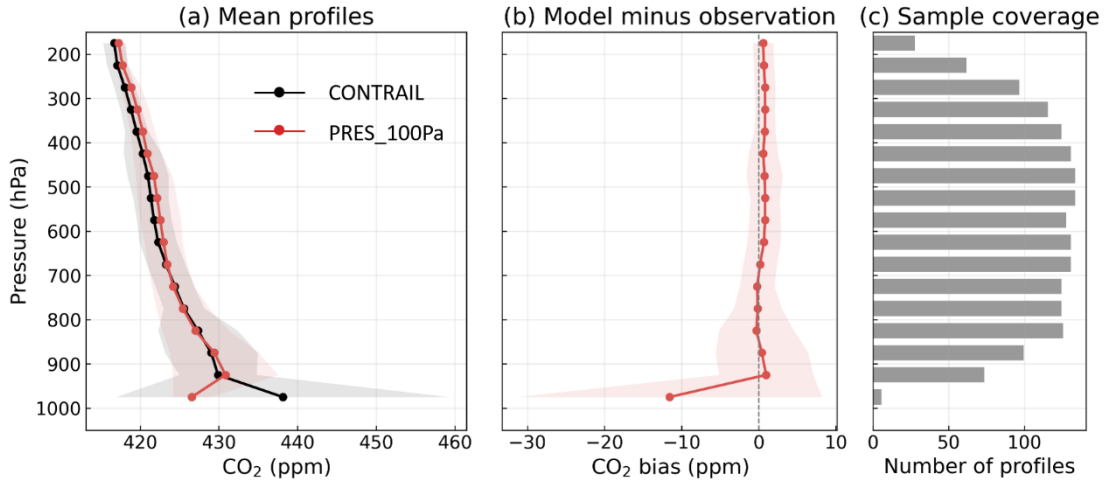


Figure S2 Comparison of CMAQ-simulated CO_2 profiles with independent CONTRAIL observations. (a) Mean CO_2 profiles. (b) Model-minus-observation biases. (c) Number of ascent/descent profiles in each 50 hPa bin. Shading indicates ±1 standard deviation across profile-bin means.

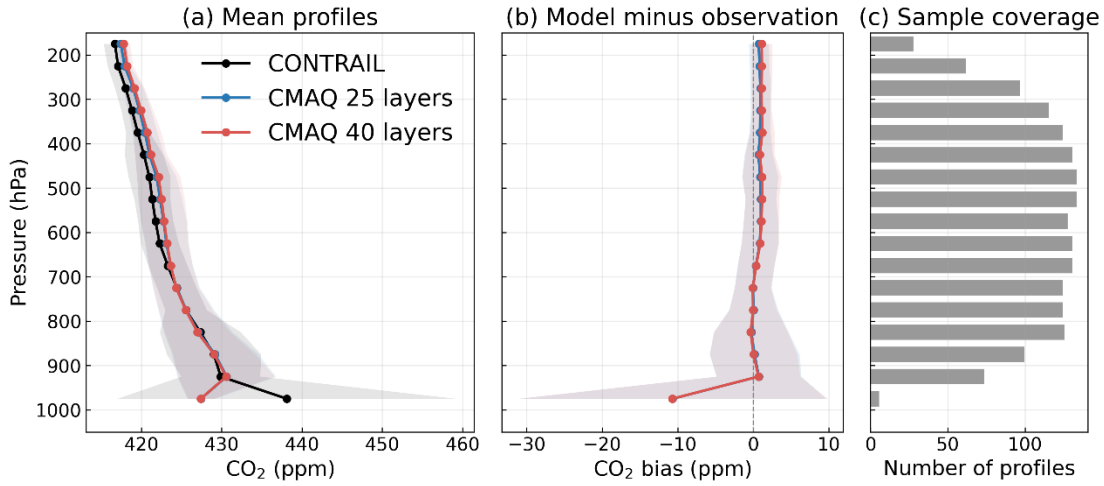


Figure S3 Comparison of CO_2 profiles simulated by the original 25-layer and refined 40-layer CMAQ configurations with CONTRAIL observations. (a) Mean CO_2 profiles. (b) Model-minus-observation biases. (c) Number of ascent/descent profiles in each 50 hPa bin. Shading indicates ±1 standard deviation across profile-bin means.

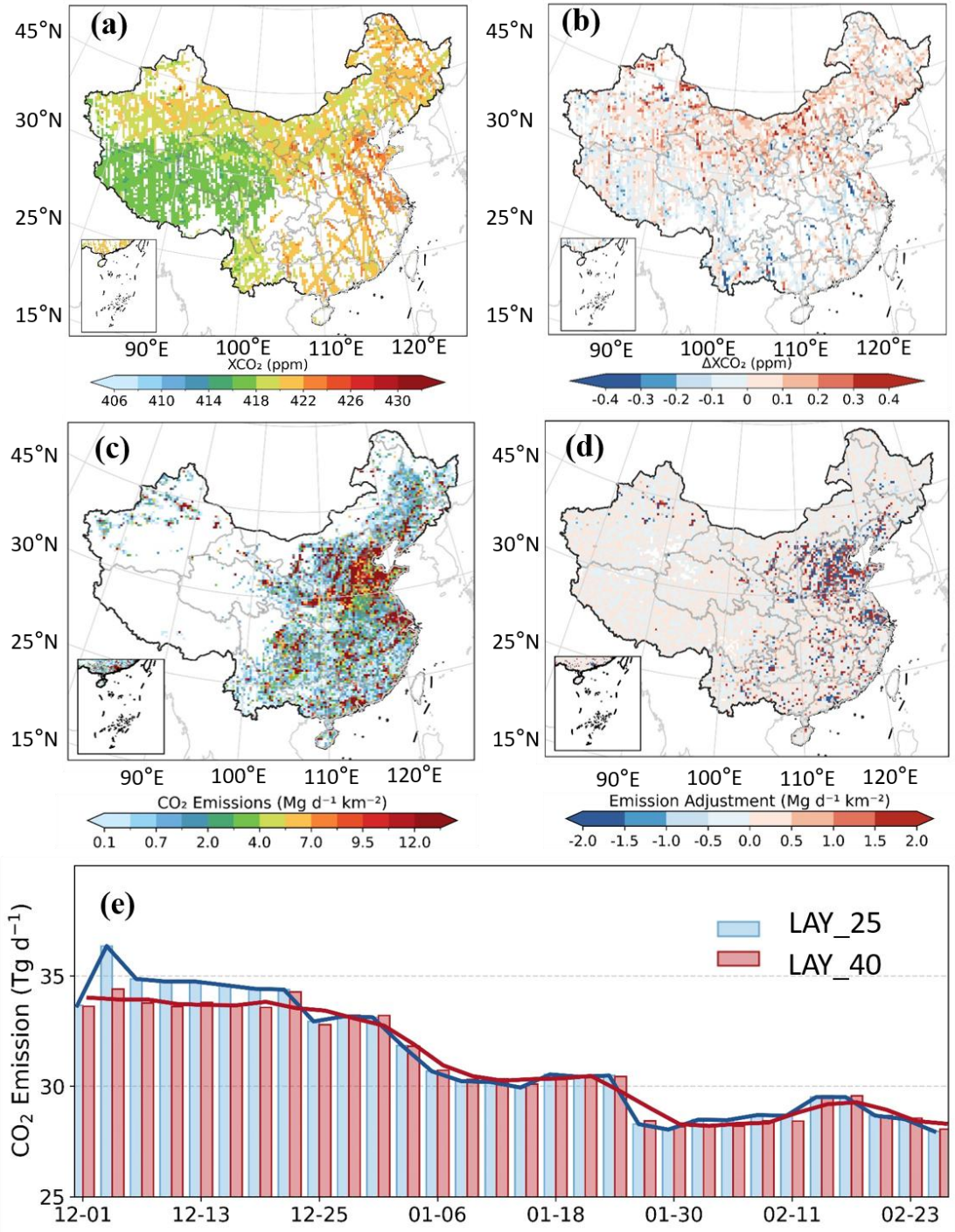


Figure S4 Sensitivity of simulated XCO_2 and posterior CO_2 emissions to vertical resolution. (a) Simulated XCO_2 and (c) posterior anthropogenic CO_2 emissions in the 40-layer experiment. (b, d) Corresponding differences from the 25-layer baseline (40-layer minus 25-layer). (e) Time series of posterior anthropogenic CO_2 emissions over China in both experiments.

2. Treatment of the atmosphere above the model top: CMAQ has a model top of 100 Pa, whereas the OCO pressure grid and pressure-weighted column extend to the top of the atmosphere. The manuscript does not explain how the CO_2 profile above the CMAQ model top is constructed when applying Eq. (4). Although this region represents only approximately 0.1% of the atmospheric column, an incorrect treatment could introduce an XCO_2 bias of up to approximately 0.4 ppm, which is comparable to the residual biases discussed in the manuscript. Please clarify whether the OCO prior profile, the uppermost CMAQ value, or another climatology is used above the model top, and whether the pressure weights are renormalized. A simple sensitivity test using alternative upper-atmospheric treatments should be reported. If the OCO prior is used above 100 Pa, this should be stated explicitly; in that case, the expected effect is likely small because the above-model contribution to the averaging-kernel correction would be zero.

Response: We appreciate the reviewer for this helpful comment. We acknowledge that the original manuscript did not clearly describe the treatment of the atmosphere above the CMAQ model top. We agree that inappropriate treatment of this region could introduce biases into simulated XCO_2. Previous studies have shown that errors in the representation of atmospheric CO_2 profiles can affect simulated column concentrations (Basu et al., 2011), and that small systematic differences in simulated XCO_2 can propagate into inferred surface fluxes (Chevallier et al., 2010). In our original inversion, the CO_2 profile above 100 Pa was taken from the prior profile associated with each OCO sounding. The original full-column pressure weights were retained without renormalization. Under the averaging-kernel formulation (Taylor et al., 2023), using the OCO prior profile in this region gives zero contribution to the profile-difference correction, while its prior contribution remains included in the full-column prior XCO_2. To assess sensitivity to this treatment, we performed an additional inversion in which the uppermost CMAQ CO_2 value was extended above 100 Pa, with all other settings unchanged. Relative to the original experiment, the sensitivity experiment yielded a mean simulated XCO_2 difference of -0.01 ppm and a root mean square difference of 0.09 ppm (Fig. S5 a-b). The fit to OCO observations remained nearly unchanged, with

RMSE values of 1.64 ppm in both experiments and biases of -0.44 and -0.45 ppm, respectively. Winter cumulative posterior anthropogenic CO_2 emissions changed by -0.6% over China, -2.1% over BTH, and +0.3% over YRD (Fig. S5 c-d). The posterior emission time series remained broadly similar, retaining the main temporal variations (Fig. S5 e). These results indicate limited sensitivity of the regional emission estimates to the two above-model-top treatments tested.

We have supplemented the description accompanying Eq. (4) to explicitly state that the OCO prior CO_2 profile is used above 100 Pa and that the full-column pressure weights are retained without renormalization. See Lines 231–256, Page 8. Details of the sensitivity experiment have been added to the Supplement.

"OCO-2/3 provides XCO_2, whereas CMAQ outputs three-dimensional CO_2 concentrations. An observation operator H is therefore required to map the model state into the satellite observation space. First, the CMAQ CO_2 vertical profile was extracted at the grid cell and model output time corresponding to each observation. The modeled concentrations were then interpolated to the OCO retrieval pressure levels. Above the CMAQ model top (100 Pa), the CO_2 profile was taken from the prior profile associated with each OCO sounding. The simulated XCO_2 was subsequently calculated by applying the OCO averaging kernel and full-column pressure weights:

$$XCO_2^m = XCO_2^a + \sum_{i=1}^{n} w_i A_i (x_i^m - x_i^a) \quad (4)$$

where XCO_2^m is the simulated XCO_2 processed by the observation operator; XCO_2^a is the prior XCO_2 from the satellite product; x_i^m and x_i^a denote the modeled CO_2 concentration and satellite prior profile at the ith retrieval layer, respectively; A_i and w_i represent the averaging kernel and pressure weight for that layer; and n is the number of satellite retrieval layers. The original OCO full-column pressure weights were retained without renormalization. Because the simulated CO_2 profile above the model top is identical to the OCO prior profile, this region contributes zero to the profile-difference correction in Eq. (4). Additionally, we conducted a sensitivity experiment using the uppermost CMAQ CO_2 value above the model top. The results

indicated limited sensitivity of regional emission estimates to the two treatments tested (see Text S3 and Fig. S5 in the Supplement)."

"**Supplement**

Text S3 Sensitivity to the treatment of CO_2 above the model top

In the reference experiment (OCO-prior), the CO_2 profile above the CMAQ model top was taken from the prior profile associated with each OCO sounding. To assess the sensitivity of the inversion to this treatment, an alternative experiment (CMAQ-top) was conducted by extending the uppermost CMAQ CO_2 value above the model top. Both experiments retained the original OCO full-column pressure weights without renormalization, and all other model and inversion settings were identical.

The simulated XCO_2 fields from the two inversion experiments showed a mean difference of -0.01 ppm and a root mean square difference of 0.09 ppm over China (Fig. S5 a-b). Their fit to OCO observations was nearly unchanged, with an RMSE of 1.64 ppm in both experiments and biases of -0.44 ppm for OCO-prior and -0.45 ppm for CMAQ-top. These XCO_2 differences reflect the combined effects of the upper-atmospheric treatment and the resulting emission adjustments. Winter cumulative posterior anthropogenic CO_2 emissions differed by -0.6% over China, -2.1% over BTH, and +0.3% over YRD. The spatial distribution of the emission differences is shown in Fig. S5d. The posterior emission time series remained broadly similar, retaining the main temporal variations (Fig. S5 e). These results indicate that the regional emission estimates have limited sensitivity to the two above-model-top treatments tested."

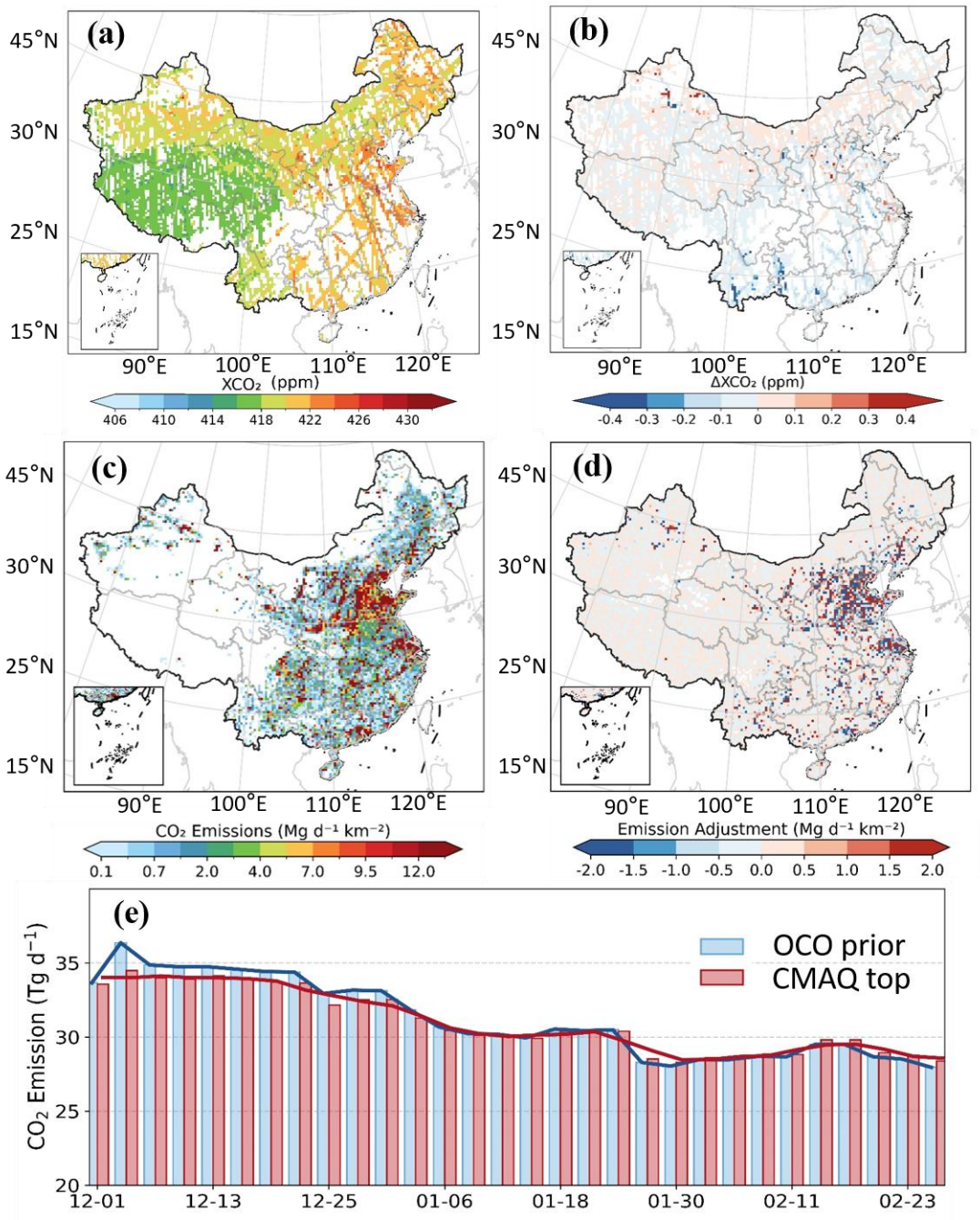


Figure S5 Sensitivity to CO_2 treatment above the model top. (a) Simulated XCO_2 and (c) posterior CO_2 emissions using the uppermost CMAQ value above 100 Pa. (b, d) Corresponding differences relative to using the OCO prior profile (CMAQ-top minus OCO-prior). (e) Posterior emission time series for both treatments.

3. The meaning of 2808.3 ± 157.0 Tg CO_2 and the 5.6% uncertainty should be reconsidered: The manuscript does not clearly define how the ±157.0 Tg CO_2 uncertainty was calculated. It appears to correspond to the 5.6% spread across the

sensitivity experiments. However, these experiments are a small set of deterministic alternative configurations rather than independent samples from a defined probability distribution. Their standard deviation therefore cannot automatically be interpreted as a posterior standard uncertainty or confidence interval.

Moreover, changing the background field and biogenic-flux product changes the national posterior estimate by -10.3% and -11.7%, respectively, both larger than 5.6%. Please provide the exact uncertainty calculation, the included error sources, any weighting scheme, and the method used to obtain the regional uncertainty values. It would be preferable to distinguish the posterior ensemble variance from structural uncertainty across model configurations and from systematic uncertainty associated with observations, transport, boundary conditions, and biogenic fluxes. In its current form, the evidence does not support statements such as "high reliability" or "reliable, operational framework."

Response: We thank the reviewer for highlighting this important issue. We acknowledge that the original manuscript did not clearly explain the calculation or interpretation of the reported uncertainty of 157.0 Tg CO_2 (5.6%). This value represented the dispersion among the selected sensitivity experiments rather than posterior ensemble uncertainty. We have therefore revised the assessment to distinguish posterior ensemble uncertainty from uncertainty associated with alternative configurations.

At the regional scale, our estimates are subject to uncertainties associated with the atmospheric CO_2 background field, prior anthropogenic emissions, biospheric carbon fluxes, model errors, background and observation error settings, and localization scale. Replacing the background field and biospheric flux product decreases posterior emissions over mainland China by 10.3% and 11.7%, respectively, relative to BASE, whereas using an alternative anthropogenic emission inventory increases the estimate by 5.7%. Sensitivity to model errors is assessed by varying the meteorological data, vertical resolution, and treatment of CO_2 concentrations above the model top. Replacing FNL with ERA5 meteorological data increases national posterior emissions by 4.9%, indicating relatively small sensitivity to meteorology-driven atmospheric transport

errors under the tested configuration. Relative to BASE, increasing the number of vertical layers from 25 to 40 decreases national posterior emissions by 0.6%. Using the CMAQ top-layer CO_2 concentration above the model top also decreases emissions by 0.6%, while setting the model top to 50 hPa decreases them by 4.6%. These results suggest relatively limited sensitivity to the tested vertical configurations. Varying the localization scale, background error settings, and observation error settings leads to absolute differences in national posterior emissions of 0.3%–1.5%, 1.4%–1.7%, and 1.5%–3.3%, respectively.

Given the high computational cost of ensemble transport simulations and inversions, comprehensively exploring all plausible uncertainty settings is impractical. Previous studies have assessed individual uncertainty contributions and combined them using an uncertainty propagation formula that neglects covariances among the contributions. Nassar et al. (2017) evaluated uncertainty using alternative wind fields, background definitions, and bias-correction approaches, with an additional contribution from secondary sources where applicable. Lin et al. (2023) assessed retrieval, wind, and background uncertainties using XCO_2 perturbations, alternative wind fields, and background thresholds, respectively. They then combined these contributions through error propagation assuming that they were uncorrelated. Feng et al. (2024) likewise estimated separate contributions from the standard deviations of emission estimates obtained by varying background-error settings, observation-error settings, meteorological fields, localization scales, and CO_2-to-NO_X emission ratios. Following these studies, we estimate the combined uncertainty σ_{emis} in regional posterior CO_2 emissions as follows:

$$\sigma_{emis} = \sqrt{\sigma_{bg}^2 + \sigma_{anth}^2 + \sigma_{bio}^2 + \sigma_{mod}^2 + \sigma_{berr}^2 + \sigma_{obserr}^2 + \sigma_{loc}^2}$$

Here, σ_{bg}, σ_{anth}, σ_{bio}, σ_{mod}, σ_{berr}, σ_{obserr}, and σ_{loc} are the standard deviations of posterior emissions obtained using different background CO_2 fields, anthropogenic emission inventories, biospheric flux products, model errors, background-error settings, observation-error settings, and localization scales, respectively. Each group includes BASE and the corresponding sensitivity experiment(s), with equal weights. For

mainland China, the overall uncertainty estimated from the tested factors is 257.7 Tg CO_2, corresponding to 9.2% of the BASE estimate. This value reflects their combined influence on posterior emissions and complements the separately reported posterior ensemble uncertainty.

Grid-level uncertainty in anthropogenic CO_2 emissions is estimated from the standard deviation across the 50 posterior ensemble members. Relative posterior ensemble uncertainty exhibits substantial spatial heterogeneity, with high values scattered across parts of northeastern and southwestern China (Fig. R3). Relatively low values, typically below 30%, occur in parts of eastern China, including portions of the North China Plain and the lower Yangtze region. These ensemble uncertainties represent the spread of emission estimates under the specified inversion configuration and depend jointly on the magnitude and correlation structure of prior errors, observational coverage, and prescribed observation errors (Wang et al., 2018; Jiang et al., 2021).

We have clarified the uncertainty calculation methods and revised the relevant statements in the manuscript.

See Lines 622–626, Page 25.

"3.3 System sensitivity and uncertainty assessment

To evaluate the sensitivity of the inversion results to different system configurations, this study conducted a series of sensitivity experiments examining background fields, model errors, observation settings, prior anthropogenic emissions, biogenic carbon fluxes, localization scales, and background and observation errors (Table 2)."

See Lines 710–714, Page 30.

"Relative to BASE, increasing the number of vertical layers from 25 to 40 (LAY_40) decreases national posterior emissions by 0.6%. Using the CMAQ top-layer CO_2 concentration above the model top (LAY_TOP) also decreases emissions by 0.6%, while setting the model top to 50 hPa (TOP_50hPa) decreases them by 4.6%."

See Lines 725–740, Page 30.

"Given the high computational cost of ensemble transport simulations and inversions, comprehensively exploring all plausible uncertainty settings is impractical. At the regional scale, we therefore followed previous studies to estimate the combined uncertainty associated with the tested factors using the following formula (Nassar et al., 2017; Lin et al., 2023; Feng et al., 2024):

$$\sigma_{emis} = \sqrt{\sigma_{bg}^2 + \sigma_{anth}^2 + \sigma_{bio}^2 + \sigma_{mod}^2 + \sigma_{berr}^2 + \sigma_{obserr}^2 + \sigma_{loc}^2}$$

Here, σ_{bg}, σ_{anth}, σ_{bio}, σ_{mod}, σ_{berr}, σ_{obserr}, and σ_{loc} represent the standard deviations of posterior emissions across configurations varying background CO_2 fields, anthropogenic priors, biospheric fluxes, model errors, background errors, observation errors, and localization scales, respectively. The model-error group covers the changes in meteorological data, vertical resolution, model-top pressure, and above-model-top CO_2 treatment described above. Each group includes BASE and the corresponding sensitivity experiment(s), with equal weights. The resulting estimate captures the combined influence of these factors on posterior emissions. For mainland China, the combined uncertainty was 257.7 Tg, 9.2% of the BASE. The uncertainties for BTH and YRD were 15.0% and 18.6%, respectively."

Table 2. Configurations of the sensitivity experiments and their posterior emission differences relative to the BASE experiment.

(a) Input data and assimilation settings

Name	BKG	Anth	Bio	Obs	Loc (km)	BKG_ Error (%)	OBS_ Error (factor)	Diff (%)
BASE	GCAS	MEIC	BEPS	O2+O3	500	40	1.0	0.0
BKG_CT	Carbon Tracker	MEIC	BEPS	O2+O3	500	40	1.0	-10.3
OBS_OCO2	GCAS	MEIC	BEPS	O2	500	40	1.0	-1.1
OBS_OCO3	GCAS	MEIC	BEPS	O3	500	40	1.0	-10.4
BIO_CASA	GCAS	MEIC	CASA	O2+O3	500	40	1.0	-11.7
EDGAR_PRI	GCAS	EDGAR	BEPS	O2+O3	500	40	1.0	+5.7
LOC_300	GCAS	MEIC	BEPS	O2+O3	300	40	1.0	-0.3
LOC_800	GCAS	MEIC	BEPS	O2+O3	800	40	1.0	-1.5
ERR_BKG0.2	GCAS	MEIC	BEPS	O2+O3	500	20	1.0	-1.4
ERR_BKG0.8	GCAS	MEIC	BEPS	O2+O3	500	80	1.0	+1.7
ERR_OBS0.5	GCAS	MEIC	BEPS	O2+O3	500	40	0.5	+3.3
ERR_OBS2	GCAS	MEIC	BEPS	O2+O3	500	40	2.0	-1.5

(b) Model-related settings

Name	Met	Layers	Top (Pa)	CO_2 above top	Diff (%)
BASE	FNL	25	100	OCO-prior	0.0
MET_ERA5	ERA5	25	100	OCO-prior	+4.9
LAY_40	FNL	40	100	OCO-prior	-0.6
LAY_TOP	FNL	25	100	CMAQ-top	-0.6
TOP_50hPa	FNL	25	5000	OCO-prior	-4.6

Note: BKG denotes inversion background field; Anth represents prior anthropogenic CO_2 emissions; Bio denotes biogenic CO_2 fluxes; Obs denotes assimilated OCO satellite observations. O2 and O3 refer to OCO-2 and OCO-3 data, and O2+O3 represents their joint assimilation. Loc is the assimilation localization scale. BKG_Error represents background error. OBS_Error denotes the prescribed observation error scaling factor. Met, Layers, and Top denote the meteorological data, number of vertical layers, and model-top pressure, respectively. OCO-prior and CMAQ-top indicate that CO_2 above the model top is taken from the OCO prior profile and the CMAQ top-layer concentration, respectively. All other settings remain identical to BASE. Diff indicates the relative difference in posterior anthropogenic emissions between sensitivity tests and the BASE case.

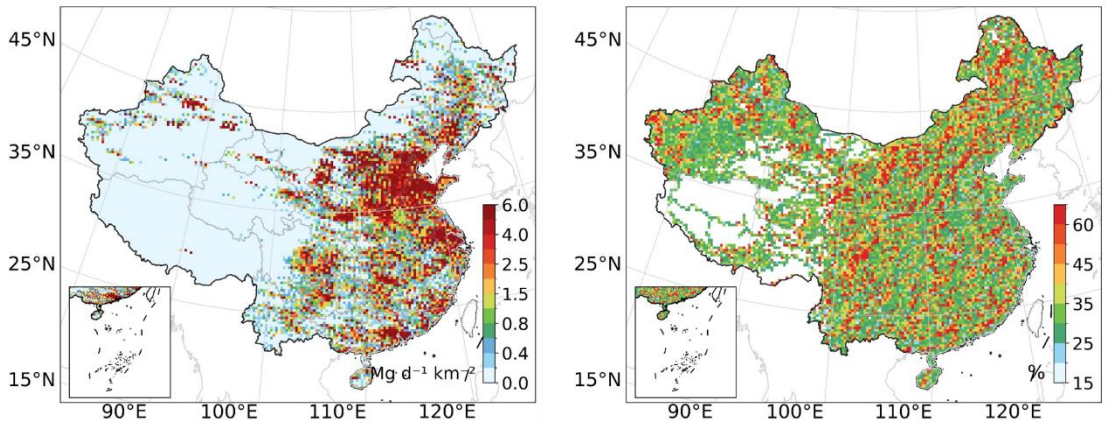


Figure R3 A posteriori CO_2 emission uncertainty at the grid scale.

Specific and minor comments

1. Inconsistent regional fractions: Section 3.1 states that BTH and YRD account for 10.8% and 16.0% of the national posterior total, respectively. However, the reported values give 294.2 / 2808.3 = 10.5% for BTH and 345.9 / 2808.3 = 12.3% for YRD. In particular, the reported YRD fraction of 16.0% is inconsistent with the stated totals. Please verify the calculation and clarify whether different denominators were used.

Response: Thank you for this careful and valuable check. We apologize for the confusion caused by the inconsistent regional fractions. Actually, the reported values of 10.8% and 16.0% in Section 3.1 were prior emission fractions, not posterior fractions. Specifically, these values were derived by dividing the BTH prior emission (260.2 Tg) and the YRD prior emission (385.9 Tg) by the national prior total (2419.3 Tg), respectively (260.2 / 2419.3 = 10.8%; 385.9 / 2419.3 = 16.0%).

We have recalculated the posterior fractions uniformly using the national posterior total of 2808.3 Tg as the denominator. The corrected values are 10.5% for BTH (294.2 / 2808.3) and 12.3% for YRD (345.9 / 2808.3). We have also checked all other reported fractions in the manuscript to ensure consistency. See Lines 420–423, Page 14.

"As two major hotspots for anthropogenic emissions, the BTH and YRD regions accounted for 10.5% and 12.3% of the national total, respectively, based on the posterior emission estimates."

2. Figure 4 panel references: The text refers to the TCCON results as Fig. 4h-i (line 447), whereas the caption lists only panels (a)-(g). Please correct the panel labels and all related cross-references.

Response: Thank you for pointing out this inconsistency. "Fig. 4h-i" in the main text is a citation error and should be corrected to "Fig. 4d-f", which corresponds to the panels actually discussed at that point in the text. Specifically, Fig. 4d-e show the comparison of simulated and observed XCO_2 at the XH and HF sites, and Fig. 4f shows the MAE of prior and posterior simulations at the two sites.

We have corrected the citation ("Fig. 4h-i" → "Fig. 4d-f") in the revised manuscript. See Lines 572-573, Page 22.

"The evaluation results at the TCCON sites show that the posterior simulations were consistently improved compared to the prior simulations (Fig. 4d-f)."

References

Basu, S., Houweling, S., Peters, W., Sweeney, C., Machida, T., Maksyutov, S., Patra, P. K., Saito, R., Chevallier, F., Niwa, Y., Matsueda, H., and Sawa, Y.: The seasonal cycle amplitude of total column CO2: Factors behind the model-observation mismatch, J. Geophys. Res. Atmos., 116, D23306, https://doi.org/10.1029/2011JD016124, 2011.

Boschetti, F., Thouret, V., Maenhout, G. J., Totsche, K. U., Marshall, J., and Gerbig, C.: Multi-species inversion and IAGOS airborne data for a better constraint of continental-scale fluxes, Atmos. Chem. Phys., 18, 9225–9241, https://doi.org/10.5194/acp-18-9225-2018, 2018.

Byrne, B., Liu, J., Bowman, K. W., Yin, Y., Yun, J., Ferreira, G. D., Ogle, S. M., Baskaran, L., He, L., Li, X., Xiao, J., and Davis, K. J.: Regional inversion shows promise in capturing extreme-event-driven CO2 flux anomalies but is limited by atmospheric CO2 observational coverage, J. Geophys. Res. Atmos., 129, e2023JD040006, https://doi.org/10.1029/2023JD040006, 2024.

Chevallier, F., Feng, L., Bösch, H., Palmer, P. I., and Rayner, P. J.: On the impact of transport model errors for the estimation of CO2 surface fluxes from GOSAT observations, Geophys. Res. Lett., 37, L21803, https://doi.org/10.1029/2010GL044652, 2010.

Deng, F., Jones, D. B. A., Walker, T. W., Keller, M., Bowman, K. W., Henze, D. K., Nassar, R., Kort, E. A., Wofsy, S. C., Walker, K. A., Bourassa, A. E., and Degenstein, D. A.: Sensitivity analysis of the potential impact of discrepancies in stratosphere–troposphere exchange on inferred sources and sinks of CO2, Atmos. Chem. Phys., 15, 11773–11788, https://doi.org/10.5194/acp-15-11773-2015, 2015.

Feng, S., Jiang, F., Wang, H., Liu, Y., He, W., Wang, H., Shen, Y., Zhang, L., Jia, M., Ju, W., and Chen, J. M.: China's fossil fuel CO2 emissions estimated using surface observations of coemitted NO2, Environ. Sci. Technol., 58, 8299–8312, https://doi.org/10.1021/acs.est.3c07756, 2024.

Jiang, F., Ju, W., He, W., Wu, M., Wang, H., Wang, J., Jia, M., Feng, S., Zhang, L., and Chen, J. M.: A 10-year global monthly averaged terrestrial net ecosystem exchange dataset inferred from the ACOS GOSAT v9 XCO2 retrievals (GCAS2021), Earth Syst. Sci. Data, 14, 3013 – 3037, https://doi.org/10.5194/essd-14-3013-2022, 2022.

Jiang, F., Wang, H., Chen, J. M., Ju, W., Tian, X., Feng, S., Li, G., Chen, Z., Zhang, S., Lu, X., Liu, J., Wang, H., Wang, J., He, W., and Wu, M.: Regional CO2 fluxes from 2010 to 2015 inferred from GOSAT XCO2 retrievals using a new version of the Global Carbon Assimilation System, Atmos. Chem. Phys., 21, 1963–1985, https://doi.org/10.5194/acp-21-1963-2021, 2021.

Kou, X., Peng, Z., Zhang, M., Hu, F., Han, X., Li, Z., and Lei, L.: The carbon sink in China as seen from GOSAT with a regional inversion system based on the Community Multi-scale Air Quality (CMAQ) and ensemble Kalman smoother (EnKS), Atmos. Chem. Phys., 23, 6719 – 6741, https://doi.org/10.5194/acp-23-6719-2023, 2023.

Lee, P., McQueen, J., Stajner, I., Huang, J., Pan, L., Tong, D., Kim, H., Tang, Y., Kondragunta, S., Ruminski, M., Lu, S., Rogers, E., Saylor, R., Shafran, P., Huang, H.-C., Gorline, J., Upadhayay, S., and Artz, R.: NAQFC developmental forecast guidance for fine particulate matter (PM2.5), Weather Forecast., 32, 343–360, https://doi.org/10.1175/WAF-D-15-0163.1, 2017.

Li, H., Zheng, B., Lei, Y., Hauglustaine, D., Chen, C., Lin, X., Zhang, Y., Zhang, Q., and He, K.: Trends and drivers of anthropogenic Nox emissions in China since 2020, Environ. Sci. Ecotechnol., 21, 100425, https://doi.org/10.1016/j.ese.2024.100425, 2024.

Li, R., Zhang, M., Chen, L., Kou, X., and Skorokhod, A.: CMAQ simulation of atmospheric CO2

concentration in East Asia: Comparison with GOSAT observations and ground measurements, Atmos. Environ., 160, 176–185, https://doi.org/10.1016/j.atmosenv.2017.03.056, 2017.

Li, S., Wang, S., Wu, Q., Zhang, Y., Ouyang, D., Zheng, H., Han, L., Qiu, X., Wen, Y., Liu, M., Jiang, Y., Yin, D., Liu, K., Zhao, B., Zhang, S., Wu, Y., and Hao, J.: Emission trends of air pollutants and CO2 in China from 2005 to 2021, Earth Syst. Sci. Data, 15, 2279 – 2294, https://doi.org/10.5194/essd-15-2279-2023, 2023.

Lin, X., van der A, R., de Laat, J., Eskes, H., Chevallier, F., Ciais, P., Deng, Z., Geng, Y., Song, X., Ni, X., Huo, D., Dou, X., and Liu, Z.: Monitoring and quantifying CO2 emissions of isolated power plants from space, Atmos. Chem. Phys., 23, 6599–6611, https://doi.org/10.5194/acp-23-6599-2023, 2023.

Machida, T., Matsueda, H., Sawa, Y., Nakagawa, Y., Hirotani, K., Kondo, N., Goto, K., Ishikawa, K., Nakazawa, T., and Ogawa, T.: Worldwide measurements of atmospheric CO2 and other trace gas species using commercial airlines, J. Atmos. Ocean. Technol., 25, 1744 – 1754, https://doi.org/10.1175/2008JTECHA1082.1, 2008.

Nassar, R., Hill, T. G., McLinden, C. A., Wunch, D., Jones, D. B. A., and Crisp, D.: Quantifying CO2 emissions from individual power plants from space, Geophys. Res. Lett., 44, 10045–10053, https://doi.org/10.1002/2017GL074702, 2017.

Niwa, Y., Machida, T., Sawa, Y., Matsueda, H., Schuck, T. J., Brenninkmeijer, C. A. M., Imasu, R., and Satoh, M.: Imposing strong constraints on tropical terrestrial CO2 fluxes using passenger aircraft-based measurements, J. Geophys. Res. Atmos., 117, D11303, https://doi.org/10.1029/2012JD017474, 2012.

Otte, T. L., and Pleim, J. E.: The Meteorology-Chemistry Interface Processor (MCIP) for the CMAQ modeling system: Updates through MCIPv3.4.1, Geosci. Model Dev., 3, 243 – 256, https://doi.org/10.5194/gmd-3-243-2010, 2010.

Pleim, J. E.: A combined local and nonlocal closure model for the atmospheric boundary layer. Part I: Model description and testing, J. Appl. Meteorol. Climatol., 46, 1383 – 1395, https://doi.org/10.1175/JAM2539.1, 2007.

Ponomarev, N., Steiner, M., Koene, E., Rubli, P., Grange, S., Constantin, L., Ramonet, M., David, L., Hamzehloo, A., Emmenegger, L., and Brunner, D.: Estimation of CO2 fluxes in the cities of Zurich and Paris using the ICON-ART CTDAS inverse modelling framework, Atmos. Chem. Phys., 26, 547–570, https://doi.org/10.5194/acp-26-547-2026, 2026.

Reichler, T., Dameris, M., and Sausen, R.: Determining the tropopause height from gridded data, Geophys. Res. Lett., 30, 2042, https://doi.org/10.1029/2003GL018240, 2003.

Taylor, T. E., O'Dell, C. W., Baker, D., Bruegge, C., Chang, A., Chapsky, L., Chatterjee, A., Cheng, C., Chevallier, F., Crisp, D., Dang, L., Drouin, B., Eldering, A., Feng, L., Fisher, B., Fu, D., Gunson, M., Haemmerle, V., Keller, G. R., Kiel, M., Kuai, L., Kurosu, T., Lambert, A., Laughner, J., Lee, R., Liu, J., Mandrake, L., Marchetti, Y., McGarragh, G., Merrelli, A., Nelson, R. R., Osterman, G., Oyafuso, F., Palmer, P. I., Payne, V. H., Rosenberg, R., Somkuti, P., Spiers, G., To, C., Weir, B., Wennberg, P. O., Yu, S., and Zong, J.: Evaluating the consistency between OCO-2 and OCO-3 XCO2 estimates derived from the NASA ACOS version 10 retrieval algorithm, Atmos. Meas. Tech., 16, 3173–3209, https://doi.org/10.5194/amt-16-3173-2023, 2023.

Verma, S., Marshall, J., Gerbig, C., Rödenbeck, C., and Totsche, K. U.: The constraint of CO2 measurements made onboard passenger aircraft on surface-atmosphere fluxes: The impact of transport model errors in vertical mixing, Atmos. Chem. Phys., 17, 5665 – 5675,

https://doi.org/10.5194/acp-17-5665-2017, 2017.
Villalobos, Y., Rayner, P. J., Silver, J. D., Thomas, S., Haverd, V., Knauer, J., Loh, Z. M., Deutscher, N. M., Griffith, D. W. T., and Pollard, D. F.: Was Australia a sink or source of CO2 in 2015? Data assimilation using OCO-2 satellite measurements, Atmos. Chem. Phys., 21, 17453 – 17494, https://doi.org/10.5194/acp-21-17453-2021, 2021.
Xian, T., and Homeyer, C. R.: Global tropopause altitudes in radiosondes and reanalyses, Atmos. Chem. Phys., 19, 5661–5678, https://doi.org/10.5194/acp-19-5661-2019, 2019.
Ye, X., Lauvaux, T., Kort, E. A., Oda, T., Feng, S., Lin, J. C., Yang, E. G., and Wu, D.: Constraining fossil fuel CO2 emissions from urban area using OCO-2 observations of total column CO2, J. Geophys. Res. Atmos., 125, e2019JD030528, https://doi.org/10.1029/2019JD030528, 2020.